

Realization of a motility-trap for active particles

Soudeh Jahanshahi¹, Celia Lozano ², Benno Liebchen³, Hartmut Löwen¹ & Clemens Bechinger ²✉

Trapping of atomic and mesoscopic particles with optical fields is a practical technique employed in many research disciplines. Developing similar trapping methods for self-propelled, i.e. active, particles is, however, challenging due to the typical anisotropic material composition of Janus-type active particles. This renders their trapping with magneto-optical fields to be difficult. Here we present the realization of a motility-trap for active particles, which only exploits their self-propulsion properties. By combining experiments, numerical simulations, and theory, we show that, under appropriate conditions, a force-free rotation of the self-propulsion direction towards the trap's center can be achieved, which results in an exponential localization of active particles. Because this trapping mechanism can be applied to any propulsion scheme, we expect such motility-tweezers to be relevant for fundamental studies of self-driven objects as well as for their applications as autonomous microrobots.

Konstanzer Online-Publikations-System (KOPS)
URL: <http://nbn-resolving.de/urn:nbn:de:bsz:352-2-13ecjwgy7kft30>

¹Institut für Theoretische Physik II: Weiche Materie, Heinrich-Heine-Universität Düsseldorf, 40225 Düsseldorf, Germany. ²Fachbereich Physik, Universität Konstanz, 78457 Konstanz, Germany. ³Institut für Festkörperphysik Technische, Universität Darmstadt, 64289 Darmstadt, Germany. ✉email: clemens.bechinger@uni-konstanz.de

The development of techniques aiming to spatially position, confine, or trap particles in space has promoted some of the most spectacular advancements in fundamental and applied science throughout the past few decades. On atomic scales, such trapping techniques have led, for example, to the realization of Bose–Einstein condensates^{1–3}, and play an important role in the development of quantum computers^{4,5} based on trapped ions. On the micron- and nanoscale, the invention of optical tweezers^{6,7} enables to exert well-controlled forces on viruses, living cells, and synthetic colloids to probe, for example, the viscoelastic properties of DNA and cell membranes, or to measure forces exerted by molecular motors^{7,8}.

An important class of particles for which effective and versatile trapping schemes are currently not available are self-propelled active particles (APs)^{9–15}. Such systems receive considerable attention due to their resemblance with motile microorganisms^{16–18}, allowing to identify general conditions under which collective behavior can emerge^{19,20}. In addition, APs are currently discussed as autonomous microrobots that may find use as autonomous vehicles to deliver loads to specific targets^{21–23}. In view of such applications, there is growing need to finely control their location in space and time, which, for example, allows to maintain high densities of APs at specific positions. Compared to Brownian particles, the application of optical traps is not straightforward, partly because APs are typically composed of nonuniform dielectric materials, including partial metallic coatings, which lead to non-isotropic optical forces and strong light scattering effects. Accordingly, present trapping mechanisms of APs require the presence of pores and walls^{24–31}, external forces^{22,23,32–39}, or the presence of other particles^{40,41}.

Here, we present a novel trapping mechanism of APs, which solely originates from their self-propulsion and does not require external forces. To demonstrate such motility trapping, we perform experiments with APs whose self-propulsion is controlled by light. We want to emphasize, however, that our results can be also applied to APs propelled by, for example, self-diffusiophoresis^{14,42} or self-thermophoresis¹⁵. Using experiments, simulations, and analytical theory, we show that a non-monotonic spatial variation of the particle's motility (exhibiting either a maximum or a minimum) leads to the localization of APs, which are unbound otherwise. To characterize this localization in detail, we introduce a trapping classification scheme by defining general criteria for “strong” and “weak” particle localization. In contrast to most other trapping mechanisms, which are less effective at high propulsion velocities, the motility trap presented here is particularly efficient for fast APs. In addition to practical implications, the presented motility traps can be also used to determine coupling coefficients of APs to external fields.

Results

Outline of the experimental approach. APs are made from colloidal silica particles with a diameter $\sigma = 3.25 \mu\text{m}$, which are half-coated with a 50-nm carbon layer on one hemisphere and afterwards suspended in a critical mixture of water and 2,6-lutidine (lutidine mass fraction 0.286). The temperature of the entire sample cell is kept constant several degrees below its lower critical point $T_c = 34.1 \text{ }^\circ\text{C}$ ^{43,44}. Due to gravity, the particles are confined to the bottom of the sample cell where they perform a two-dimensional motion. Under laser illumination ($\lambda = 532 \text{ nm}$), light is mainly absorbed at the carbon cap, leading to the preferential heating of the cap. Once the cap temperature exceeds, T_c , this results in a local demixing of the adjacent fluid. In our experiments, such conditions are achieved above a threshold intensity of $I_0 \sim 0.08 \mu\text{W } \mu\text{m}^{-2}$. Depending on the light intensity, the demixing region is characterized by a single or (at higher intensities) two single-phase droplet(s) that nucleate around the

particle. The droplet's asymmetrical shape leads to a propulsive velocity v , which depends on the light intensity in a strongly non-monotonic fashion (Fig. 1a)^{43,45}. While v linearly increases at sufficiently low intensities, it sharply reverses its direction \mathbf{n} relative to the cap above a certain intensity threshold $I_r \sim 0.58 \mu\text{W } \mu\text{m}^{-2}$ when a second droplet covers the uncapped surface (see Fig. 1a and “Methods” for details). Due to the additional presence of rotational diffusion ($D_r \sim 1/50 \text{ s}$), the APs perform an unbiased persistent random motion under homogeneous illumination conditions.

In the presence of a light gradient ∇I , the shape of the nucleating droplets around the APs is no longer symmetric relative to \mathbf{n} . As a consequence, AP motion becomes strongly biased leading to a phototactic behavior⁴³. Depending on whether the illumination intensity is below or above I_r , APs will

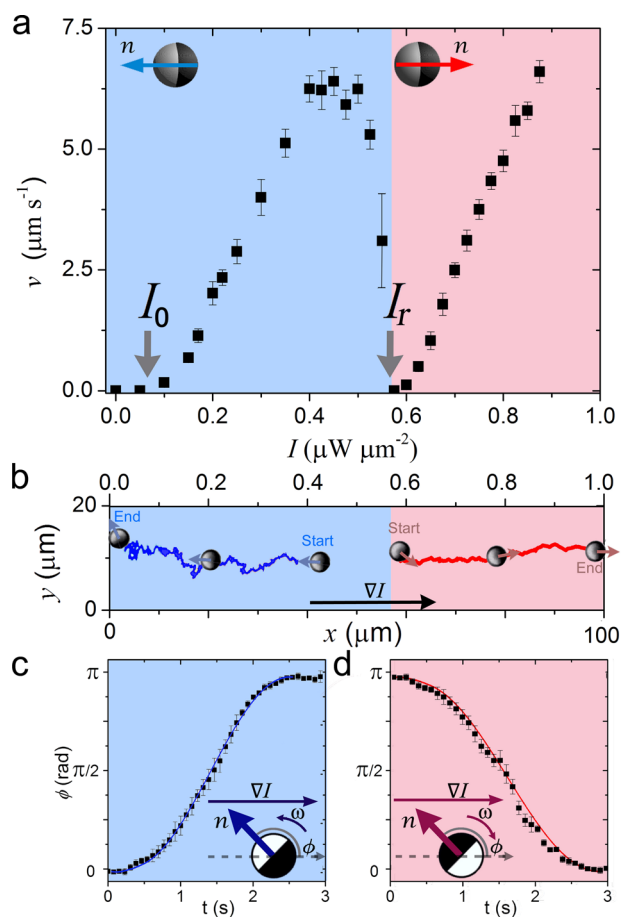


Fig. 1 Light-activated motion. **a** Measured propulsion velocity v of the active particle (AP) vs. illumination intensity I . Above a threshold intensity $I_0 \sim 0.08 \mu\text{W } \mu\text{m}^{-2}$ the propulsion mechanism sets in, leading to self-propulsion. The vector \mathbf{n} corresponds to the direction of propulsion and reverses its sign at the critical intensity I_r . **b** Example of measured trajectories of an AP in a static light gradient ∇I . Below I_r , the AP moves opposite to ∇I (negative phototaxis, blue trajectory and background). Above I_r , the particle moves along ∇I (positive phototaxis, red trajectory and background). Time evolution of the angle ϕ between the propulsion direction of the AP and the direction of the light gradient, after the AP is suddenly exposed to the light gradient for intensities **c** below I_r and **d** above I_r . Squares denote averaged data, and the full line shows the theoretical fits. In both cases, an identical light gradient of intensity $|\nabla I| = 0.1 \mu\text{W } \mu\text{m}^{-3}$ was used. Inset: Sketch of an AP in a positive and negative light gradient together with the resulting angular velocity ω at which the AP rotates when the light gradient is switched on. Error bars denote the standard deviation.

experience an aligning torque leading to their propulsion opposite (negative phototaxis) or along ∇I (positive phototaxis), respectively (Fig. 1b). To characterize the particle's alignment, we have measured their reorientation dynamics within a light gradient. Experimentally, this was achieved by suddenly turning on a light gradient in x -direction when the particle propulsion direction \mathbf{n} was pointing along the positive x -direction (dashed line in the insets of Fig. 1c). As a result of the droplet's asymmetry, the particle will realign until \mathbf{n} is antiparallel (negative phototaxis) or parallel (positive phototaxis). This orientation process is shown in Fig. 1c, with ϕ being the angle between \mathbf{n} and the x -direction (see inset).

Theoretical model. To describe our experimental findings, we consider the motion of an overdamped self-propelled particle whose propulsion velocity $v(x)$ varies in space and which can align parallel or antiparallel to the local intensity gradient depending on the tactic condition. This leads to the following Langevin equations for the center of mass position $\mathbf{r}(t) = (x(t), y(t))$ and the self-propulsion direction $\mathbf{n} = (\cos(\phi), \sin(\phi))$ expressed by its angle ϕ with the x -axis (see ref. ⁴⁶ for details)

$$\dot{\mathbf{r}}(t) = v(x)\mathbf{n} + \sqrt{2D}\boldsymbol{\xi}(t), \quad (1)$$

$$\dot{\phi}(t) = \omega(\phi, x) + \sqrt{2D_r}\xi_\phi. \quad (2)$$

Here, $\boldsymbol{\xi}(t) = (\xi_x(t), \xi_y(t))$, $\xi_\phi(t)$ describe Gaussian white noise, with zero mean and unit variance, and D and D_r correspond to the translational and rotational diffusion coefficients, respectively.

As will be later shown in our experiments, the key mechanism for the motility trap is the active alignment of APs relative to the local intensity gradient. The instantaneous alignment rate ω depends on both the surface-averaged total velocity of the solvent around the AP and its asymmetry relative to the AP orientation⁴⁷. Since the magnitude of the surface-averaged flow velocity also controls the self-propulsion speed⁴⁷, on the one hand, we expect $\omega \propto v$. On the other hand, the dependence of ω on the flow field asymmetry suggests $\omega \propto |\nabla I|$ or $\omega \propto v'(x) = dv(x)/dx$. This leads

to the following overall expression for the phototactic alignment rate $\omega(\phi, x) = \frac{c}{\sigma} v(x) v'(x) \sin \phi$ (see ref. ⁴⁶ regarding the determination of the coefficients). Here, we have introduced the particle diameter σ occurring in the denominator since alignment competes with the rotational drag, the latter linearly scaling with σ . Finally, the coefficient c , a parameter fixed by experiments, determines if phototaxis is positive ($c < 0$) or negative ($c > 0$) (see "Methods" for further details). With this form for the alignment rate, the orientational dynamics, as obtained from the noise-free solution of (1) and (2), is in good agreement with the experimental observations, see Fig. 1c, d.

Realization of an AP motility trap. A motility trap requires a position-dependent AP realignment mechanism, which prevents it from leaving a certain spatial region. In our experiments, this is achieved by a spatial light profile, which is created by periodically scanning a line-shaped laser beam with a mirror across the sample plane (see "Methods"). Synchronization of the mirror motion with an electro-optical intensity modulator yields to illumination of APs with arbitrary one-dimensional illumination profiles (Fig. 2a). Since the scanning frequency of the mirror is set to 200 Hz, this leads to quasi-static illumination conditions for the APs. In our experiments, we created triangular-shaped intensity fields with either an intensity minimum (Fig. 2b) or an intensity maximum (Fig. 2c), each characterized by the width of l_v , which has been varied between 8 and 300 μm . The profile in Fig. 2b varies between $I = 0.08$ and $0.4 \mu\text{W} \mu\text{m}^{-2}$, with the intensity minimum located at $x = 0$. Since the intensities are below I_r , under such conditions APs will always align towards the intensity minimum, that is, opposite to ∇I (see Fig. 1b). Conversely, for the profile shown in Fig. 2c, the intensity varies between $I = 0.58$ and $0.9 \mu\text{W} \mu\text{m}^{-2}$, with the maximum at $x = 0$. Because this intensity range is above I_r , here APs align towards the intensity maximum, that is, parallel to ∇I (see Fig. 1b).

We start by a qualitative discussion of the experimental results for the conditions shown in Fig. 2b. In addition to affecting the alignment of APs, a position-dependent light field $I(x)$ leads to a spatial variation of self-propulsion velocity $v(x)$ shown in Fig. 2d.

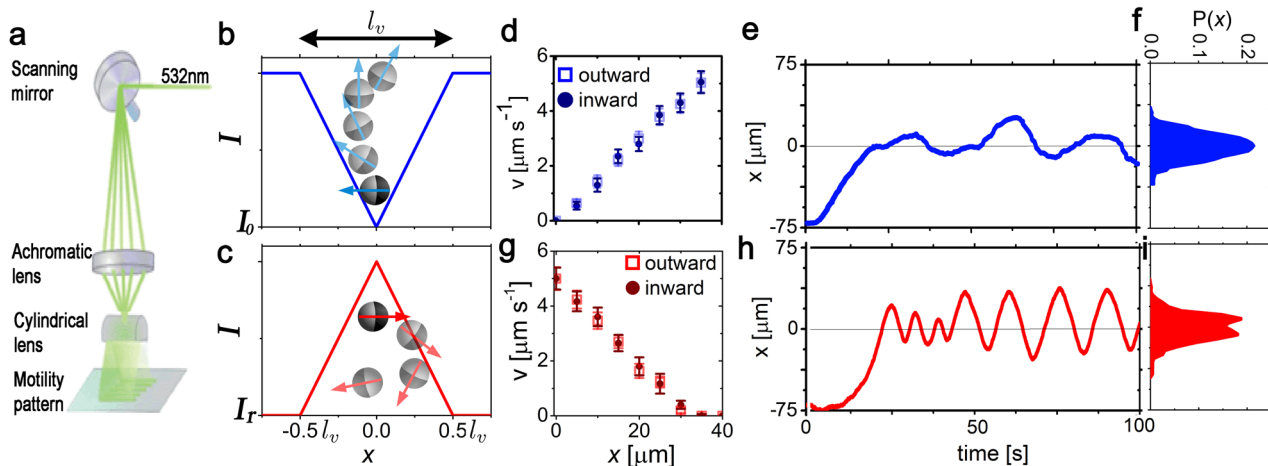


Fig. 2 Experimental realization of a motility trap. **a** Sketch of experimental setup. **b** Spatial intensity profile of a "cooling trap." The blue line describes the intensity profile of a one-dimensional triangle-shaped light field with period length $l_v = 150 \mu\text{m}$. The intensities are within the range where the particle displays negative phototaxis, that is, above the threshold intensity I_0 , but below the critical intensity I_r . Superposed are subsequent snapshots of a typical active particle's (AP) dynamics in such a trap, where the blue arrow describes the direction of motion of the particle. **c** Same as in **b** but for a "heating trap": the red line describes the intensity profile of the light field, which is in the range of positive phototaxis, that is, above the critical intensity I_r . For a cooling trap: **d** shows the x -component of the active particle's velocity, $v(x)$, for outward motion (empty squares) and inward motion (filled circles); **e** shows an example of an AP's trajectory relative to the trap center (horizontal line at $x = 0$), and **f** its positional probability distribution $P(x)$. For a heating trap, the corresponding **(g)** inward and outward velocities $v(x)$ **(h)** AP typical motion relative to the trap center, and **i** its $P(x)$. Error bars correspond to the standard deviation.

The values of $v(x)$ were obtained from the spatially resolved analysis of the particle's trajectories and agree with the values shown in Fig. 1a considering a piecewise linear intensity profile (Fig. 2b). To rule out the possible influence of optical forces acting on the APs, $v(x)$ was independently determined for the inward (towards $x = 0$) and outward (away from $x = 0$) particle motion. The data show the identical results, which confirm the absence of optical gradient forces in our experiment.

The dynamics of the AP within the intensity profile is shown in Fig. 2e. When the particle propels away from the intensity minimum, the light gradient reverses its self-propulsion direction, thus leading to an effective trapping mechanism. Because the AP cannot instantaneously change its orientation but with a rate which is limited by viscous friction, it significantly overshoots the trapping center, which causes the oscillations around the trapping center seen in Fig. 2e. This spatial confinement is confirmed by the corresponding particle probability distribution function (PDF) (Fig. 2f). Since the AP becomes localized around the position where $v(x)$ is smallest, in the remainder we refer to such conditions as a “cooling trap,” in analogy to cold atoms remaining in the vicinity of the minimum of an optical trap⁴⁸.

In addition, we also performed similar measurements for the light field shown in Fig. 2c, which features a maximum in the center and where the intensities are above I_r . Then, the APs exhibit a positive phototactic response, that is, its swimming motion is biased in the direction of ∇I . As for the cooling trap, the AP's velocity linearly depends on the local light intensity (Fig. 2g), but with the trajectory now being localized around the

intensity maximum (Fig. 2h), which spatial confinement is confirmed by its $P(x)$ (Fig. 2i). Since $v(x)$ is largest at these regions, this explains why the oscillations become significantly enhanced compared to Fig. 2e. In the following, we refer to such trapping conditions as a “heating trap.”

As already discussed, the spatial confinement of APs within a motility trap is governed by their orientational response to the light gradient. We quantify this in Fig. 3a, b by plotting the characteristic alignment time τ , defined as the time needed for a rotation of the AP between $\phi = 0.14$ and 3 rad, as a function of $|\nabla I|$ (see “Methods” for further details). The alignment time monotonically decreases with increasing $|\nabla I|$. In addition, τ decreases when I increases (apart near I_r , where the AP motion becomes unstable) because of the stronger solvent flow near the particle⁴⁶. This latter dependence also explains why the reorientation dynamics for the cooling trap is slower than that of a heating trap (Fig. 2e, h).

To obtain the relationship between the alignment time and the widths of the particle PDFs within the motility traps, we have varied the intensity profile width l , which leads to different intensity gradients. The resulting PDF for the cooling and the heating trap both show a maximum at the trap center with exponentially decaying tails at both sides. As expected, the localization becomes more efficient when the alignment time τ becomes faster, that is, when $|\nabla I|$ increases (symbols in Fig. 3c, d). The observed shape of the PDF is in stark contrast to an AP without active alignment where it simply follows an effective Boltzmann distribution⁴⁹.

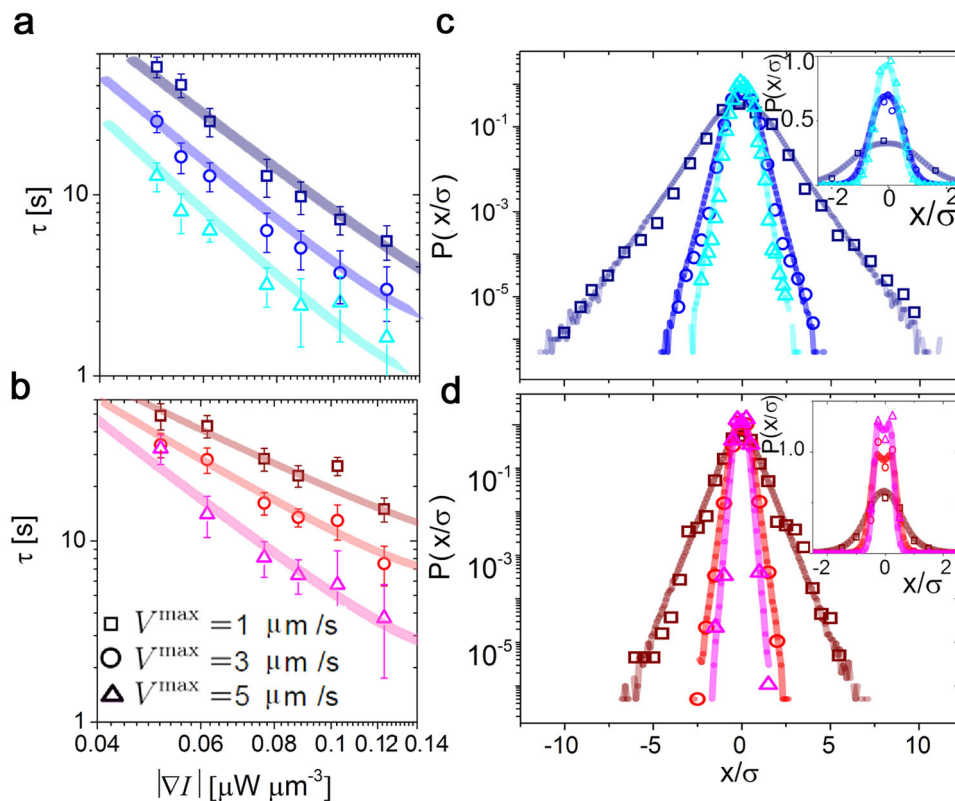


Fig. 3 Localization of active particles (APs) in a motility trap. The data for a cooling and a heating trap are shown in **a, c** and **b, d**, respectively. Symbols and solid lines show experimental data and numerical simulations, respectively. In each plot, different symbols and the curve of the corresponding color correspond to light profiles with different laser intensities, characterized by the largest velocity V^{max} achieved by active particles within each profile. **a, b** Alignment time τ of an AP as a function of the intensity gradient $|\nabla I|$ for different laser intensities. The solid curves show the theoretical fit according to $\tau = \frac{2\tilde{C}}{|\nabla I|} \ln\left(\frac{\cos(\phi_{\text{max}}) + 1}{\sin(\phi_{\text{max}})}\right)$, where \tilde{C} is the fitting parameter and the total rotation $\phi_{\text{max}} = 3$ rad. Experimental data are averaged over 10 repetitions for each curve. **c, d** Corresponding probability distribution function of the particle's position (x) rescaled by the particle size (σ) in log-lin and (as inset) lin-lin scale. Error bars correspond to the standard deviation.

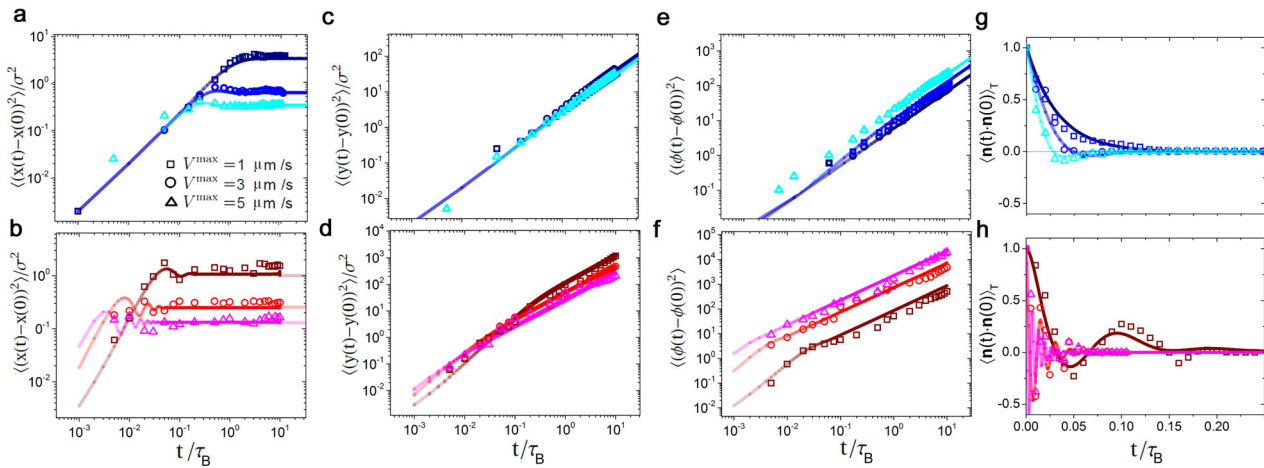


Fig. 4 Dynamical response of active particles. The data for a cooling and a heating trap are shown in **a, c, e, g** and **b, d, f, h**, respectively. Symbols and solid lines show experimental data averaged over five repetitions for each curve and numerical simulations, respectively. In each plot, different symbols and the curve of the corresponding color correspond to light profiles with different laser intensities, characterized by the maximal velocity V^{\max} achieved by active particles within the corresponding profile. Panels show the mean-square displacement in units of the particle size (σ) (**a, b**) along the x component, (**c, d**) and the y component, while **e, f** along the angular component (ϕ), and **g, h** the orientational autocorrelation function. All quantities are a function of time in units of typical Brownian time τ_B .

As a first test of the validity of our theoretical model, we now determine the PDF of APs in the trap by performing Brownian dynamics simulations for an ensemble of particles, initialized in the vicinity of the trapping center, with random initial conditions. As shown in Fig. 3c, d (solid lines), the resulting distributions are in quantitative agreement with our experiments. For positive phototaxis, we obtain a comparatively high propulsion velocity near the trap center (“heating”); in contrast, the velocity is smallest near the trapping center for the “cooling” trap. In both cases, the particle distribution decays exponentially as the distance from the center decreases (Fig. 3c, d), which leads to a saturation of the mean-square displacement, see Fig. 4a, b.

To further characterize the properties of the motility trap, we also perform analytical calculations to determine the steady-state particle distribution. For weak noise, this yields the following approximate expression for the PDF (see “Methods” for calculation details):

$$P(x) \simeq \frac{\pi^{-1} \left| \frac{dB(x)}{dx} \right|}{\sqrt{1 - B^2(x)}}, \quad B(x) = \exp\left(-\frac{c}{\sigma}(v(x) - v(0))\right). \quad (3)$$

Here the B^2 term in the denominator of Eq. (3) is mainly relevant near the trapping center $x = 0$.

Since $B(x)$ decays faster in x for small particle-size (σ) values than for large ones, it follows from Eq. (3) that the tails of the PDF decay faster in x for small particles. This corresponds to the fact that $\omega \propto 1/\sigma$ in Eq. (2), mirroring the fact that larger APs turn slower in a given gradient than small APs. In addition, Eq. (3) shows that the tails of the PDF decay faster as the slope of the gradient increases. Physically, this is because steep gradients bias the propulsion direction of APs more efficiently towards the trapping center than shallow gradients.

Mean-square displacement and dynamical correlations. To characterize the AP dynamics within a motility trap, we now perform Brownian dynamics simulations of our model (details in “Methods” section) and compare our results with experiments. This leads to a close quantitative agreement without any adjustable fitting parameters (see Fig. 4).

We first discuss the translational and rotational mean-square displacement (Fig. 4). Notice first that there is a plateau occurring

in the mean-square displacement $\langle (x(t) - x(0))^2 \rangle$, which represents (permanent) trapping in x direction. That is, we can define (the square of) a length scale corresponding to the confinement length by

$$\langle x^2 \rangle = \int dx x^2 P(x). \quad (4)$$

The confinement length decreases as the depth of the trap V^{\max} increases.

In Fig. 4b, we observe peaks preceding the onset of the plateau. These peaks correspond to the average time an AP needs for a “roundtrip” in the trap, which we denote with \bar{T}_{osc} . Accordingly, the time between $t=0$ and the first maximum of $\langle (x(t) - x(0))^2 \rangle$ is $\bar{T}_{\text{osc}}/2$.

For example, particles that are close to the trapping center at a given time move ballistically outwards and, afterward, reach their turning point after a characteristic typical time amounting roughly to $\bar{T}_{\text{osc}}/2$, before they move back towards the trapping center.

The mean-square displacement is comparatively large at the time where most particles are close to their turning point, leading to a local maximum in Fig. 4b. Then, the particles turn and propel back towards the trapping center, leading to a minimum in Fig. 4b. The particles cross the trapping center, moving outwards again and so on, leading to a sequence of further peaks that are smaller than the first one (“damped oscillations”), because particles do not reach the turning point at exactly the same time. This effect is far less pronounced for negative phototaxis (cooling trap), where particles are slow in the vicinity of the trap’s center and already reach their first turning point at significantly different times. Therefore, oscillations are barely visible in this case, see Fig. 4a.

Since the APs translate and rotate in unbounded space along the y and ϕ direction, no oscillations occur in the mean-square displacements $\langle (y(t) - y(0))^2 \rangle$ (see Fig. 4c, d) and $\langle (\phi(t) - \phi(0))^2 \rangle$ (see Fig. 4e, f).

To quantify the impact of the light field (trap) on the orientational correlation of the APs, we consider the following

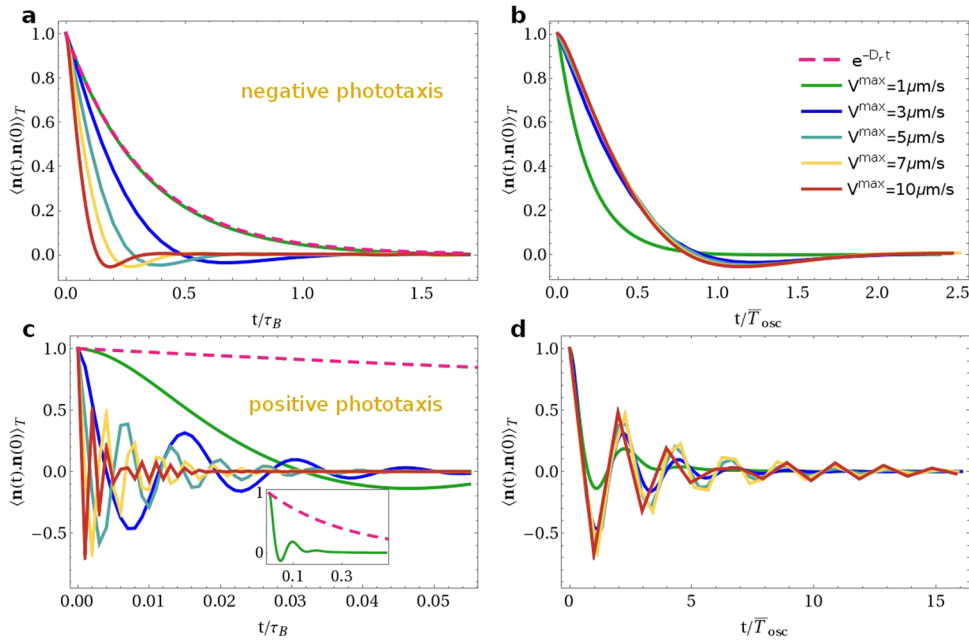


Fig. 5 Orientational autocorrelations of an active particle in a motility trap. Results from numerical simulations for a cooling trap (**a, b**) and for a heating trap (**c, d**), respectively. In all cases, the trap length is set to $l_v = 46.15 \sigma$ in units of active particle (AP) diameter σ , and the minimal velocity $v^{\min} = 0$. The active torque is tuned by choosing $c = +0.6$ and $-1.2 \tau_B$ for the cooling and the heating trap, respectively, in units of the typical Brownian time τ_B . **a, c** Decay of the orientational autocorrelation function of an active particle (AP) as a function of time in units of the Brownian time τ_B . Solid lines correspond to different propulsion velocities as specified in the legend of **b**. For comparison, we also show the data in absence of an active torque, that is, $c = 0$ (dashed magenta line). The inset in **c** shows the same data on a larger timescale. **b, d** Same data as before but with the timescale in units of the corresponding oscillation time \bar{T}_{osc} .

correlation function:

$$\langle \mathbf{n}(t) \cdot \mathbf{n}(0) \rangle_T = \lim_{T \rightarrow \infty} \frac{1}{T} \int_0^T dt' \mathbf{n}(t+t') \cdot \mathbf{n}(t'). \quad (5)$$

In the absence of the motility trap orientational correlations decay exponentially at a time scale determined by the inverse rotational diffusion time $1/D_r$. As shown in Fig. 4g, h, the motility trap induces a faster decorrelation, mirroring the fact that the light gradients that are responsible for phototaxis, and hence for motility trapping, systematically bias the AP's self-propulsion direction towards the trapping center.

Notably, when the orientational correlation time is larger than the oscillation time \bar{T}_{osc} , we even observe negative correlations (see Fig. 5). To see how such negative correlations can occur, consider a particle which is in the center of the trap at $t=0$ (or some other time) and which moves outwards shortly afterward. When the particles reach its turning point around $t \sim \bar{T}_{\text{osc}}/2$, before losing information about its orientation at time t , there is an enhanced probability that it moves back towards the trapping center at times $t \gtrsim \bar{T}_{\text{osc}}/2$, leading to negative orientational correlations.

Delocalization vs. weak and strong localization. Let us now further characterize the trapping properties of motility traps by defining a formal classification of localization scenarios, signatures of which we will then associate with APs in motility traps. We therefore consider a trap of length l_v and depth $\Delta v = v^{\max} - v^{\min}$ in a box of size L (with periodic boundary conditions), leading to a piecewise linear particle velocity $v(x)$ as shown in Fig. 6a. (Note that from here onwards we allow for a nonzero v^{\min} , which avoids that particles get stuck at the trap bottom in the noise-free special case.) This trap creates an effective active torque $\omega(\phi, x)$ acting on phototactic APs inside the trap

($|x| < l_v/2$), where $v'(x) \neq 0$, while particles at $|x| \geq l_v/2$ show unbiased active (Brownian) motion.

We now define three idealized localization scenarios, which we call (i) delocalization, (ii) weak localization, and (iii) strong localization. To do this, we keep l_v constant and explore the behavior of the squared width of the particle distribution around the trap center, $\langle x^2 \rangle$, as defined in Eq. (4), in the limit of large L , ∇v . The first scenario, delocalization, is defined by

$$\lim_{L \rightarrow \infty} \lim_{\nabla v \rightarrow \infty} \frac{\langle x^2 \rangle}{l_v^2} = \lim_{\nabla v \rightarrow \infty} \lim_{L \rightarrow \infty} \frac{\langle x^2 \rangle}{l_v^2} \rightarrow \infty. \quad (6)$$

Signatures of delocalization only occur in the absence of an active torque for an ensemble of APs, that is, for cases where the light pattern only affects the speed of the particles. Then, noise-free APs move persistently in the direction of their initial orientation and never turn so that $\langle x^2 \rangle$ diverges as L diverges, independently of ∇v . In general, noise additionally contributes to delocalization.

The next scenario, weak localization, is defined by

$$\lim_{L \rightarrow \infty} \lim_{\nabla v \rightarrow \infty} \frac{\langle x^2 \rangle}{l_v^2} = 0 \neq \lim_{\nabla v \rightarrow \infty} \lim_{L \rightarrow \infty} \frac{\langle x^2 \rangle}{l_v^2} \rightarrow \infty. \quad (7)$$

This scenario applies if particles are localized in a single point when $\Delta v \rightarrow \infty$ (then the inner limit on the left side of (7) is zero), but they can leave the trap with a finite probability when Δv is finite. In the latter case, particles that have left the trap can freely explore the available space and hence $\langle x^2 \rangle$ diverges as L diverges such that the limit on the right-hand side (r.h.s.) of (7) is infinite.

Signatures of weak localization are expected to occur for APs in a motility trap of finite depths, even in the presence of noise. This is because motility traps create an exponential localization with a localization length that essentially decreases linearly with Δv (see “Methods” section). Thus, $\langle x^2 \rangle$ decreases exponentially in Δv as Δv increases, but $\langle x^2 \rangle$ increases only as L^2 when L increases. It

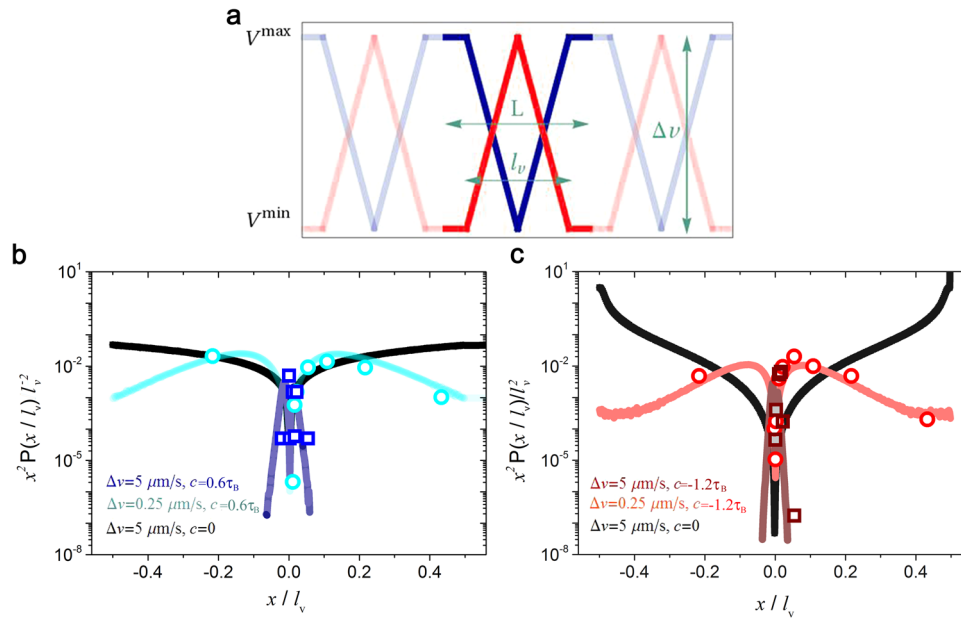


Fig. 6 Comparison of localization in cooling and heating trap. **a** Spatial propulsion velocity profile of an active particle (AP) inside a cooling trap (blue line) and a heating trap (red line). Light-colored lines indicate the periodic boundary conditions considered in the numerical simulations (within a box of size L). Profiles are characterized by their period length l_v and the propulsion velocity variation $\Delta v = V^{\max} - V^{\min}$, where V^{\max} and V^{\min} correspond to the maximal and minimal velocity within each profile. **b, c** As a measure of AP localization within each trap, we plot $x^2 P(x/l_v)/l_v^2$ as a function of x/l_v for the cooling (**b**) and heating (**c**) trap, respectively. Here x is the particle position relative to the trap center ($x=0$) and $P(x/l_v)$ indicates the positional probability distribution in units of l_v . Symbols and solid lines correspond to experimental data and numerical simulations, respectively. The data correspond to the specific situation where $L = l_v = 46.15 \sigma$, with σ the AP diameter. In all cases, we have chosen $V^{\min} = 0$. Different colors correspond to different values of Δv in the presence ($c \neq 0$) and in the absence of an active torque ($c = 0$) as specified in the legends of the typical Brownian time τ_B .

follows that first increasing Δv and then L exponentially reduces the fraction of particles, which significantly contribute to $\langle x^2 \rangle$ compared to the case where L is first increased, such that the two limits in (7) do not interchange.

Finally, the case where both limits interchange and equal zero

$$\lim_{L \rightarrow \infty} \lim_{\Delta v \rightarrow \infty} \frac{\langle x^2 \rangle}{l_v^2} = \lim_{\Delta v \rightarrow \infty} \lim_{L \rightarrow \infty} \frac{\langle x^2 \rangle}{l_v^2} = 0, \quad (8)$$

defines “strong localization.” This case occurs if particles cannot reach regions beyond l_v even in a trap of finite depth. Such a scenario strictly applies only to noise-free APs in a motility trap with a size l_v , which is larger than (twice) the distance between the trapping center and the turning point of the trajectories. Note that specifically in the present quasi-1D setup, the distance between the turning point of an AP and the trapping center depends on its initial orientation. Thus, strong localization would only occur for noise-free AP ensembles with initial angles prepared in the interval $\varphi_e \leq \phi_0 \leq \pi - \varphi_e$, with $\varphi_e = \text{const}$ larger than the critical angle $\arcsin(e^{-|c|\Delta v/\sigma})$ (see “Methods”), leading to turning points inside the trap.

In our simulations and experiments, where noise is present and traps have a finite depth, we still find notable signatures of these localization scenarios, both for positive and negative phototaxis. A first indication of this can be seen from Fig. 6b, c revealing that the maximum of $x^2 P(x)$ lies outside the trap ($|x| \geq l_v/2$) in the absence of an active torque (yielding a signature of “delocalization”), whereas in the presence of an active torque, the maximum of $x^2 P(x)$ typically lies inside the trapping region ($|x| < l_v/2$). In particular, for steep but finite traps ($\Delta v = 5 \mu\text{m s}^{-1}$, dark shades of blue and red in Fig. 6b, c) typical particle ensembles explore only a small region around the trapping center, but not the vicinity of the trap. Conversely, for $\Delta v = 0.25 \mu\text{m s}^{-1}$ (light shades of blue and red in Fig. 6b, c), $x^2 P(x)$ features a significant tail outside the considered trapping region. Only this latter fraction of particles can explore the space outside the trap

and provides a major contribution to $\langle x^2 \rangle$ when L would increase. To relate these observations to the above-defined localization scenarios, we now systematically study the parameter dependence of $\langle x^2 \rangle$.

In Fig. 7a, b, we consider APs in the absence of an active torque. Here $\langle x^2 \rangle$ generally gets larger and larger when increasing L , independently of the value of Δv , which is consistent with our definition of delocalization. In contrast, in Fig. 7e, f (deep trap), $\langle x^2 \rangle$ decreases to a value near zero as Δv increases and does not notably change when L increases. This can be viewed as a signature of strong localization, occurring for a typical particle ensemble in a sufficiently steep motility trap, which is observed over some typical finite time of a few hundred particle oscillations in the trap. Note that strong localization can of course never strictly apply in the presence of noise, because at any finite trap depth fluctuations would transfer the AP out of the trap after a sufficiently long time; here, far beyond the timescale of our simulations and experiments. Therefore, we view the present findings as signatures of strong localization. Finally, following Fig. 7c, d, when Δv increases first, $\langle x^2 \rangle$ decreases to smaller and smaller values and is then largely insensitive to subsequent changes of L . Note that increasing Δv beyond values shown on the y -axis of the middle panels, one reaches the regime shown in Fig. 7e, f, where $\langle x^2 \rangle$ does not significantly change when increasing L . Conversely, when first increasing L in Fig. 7c, d, $\langle x^2 \rangle$ gets larger and larger and ultimately diverges, as expected for weak localization.

Possible application. Besides the obvious value of motility traps as a novel tool to controllably localize or displace APs, here we discuss how they might also become useful in the future as a new tool to measure coupling coefficients of APs to external field gradients (or phoretic gradients produced by other particles). A direct measurement is not straightforward because the APs response to external fields is a superposition of fluctuations and

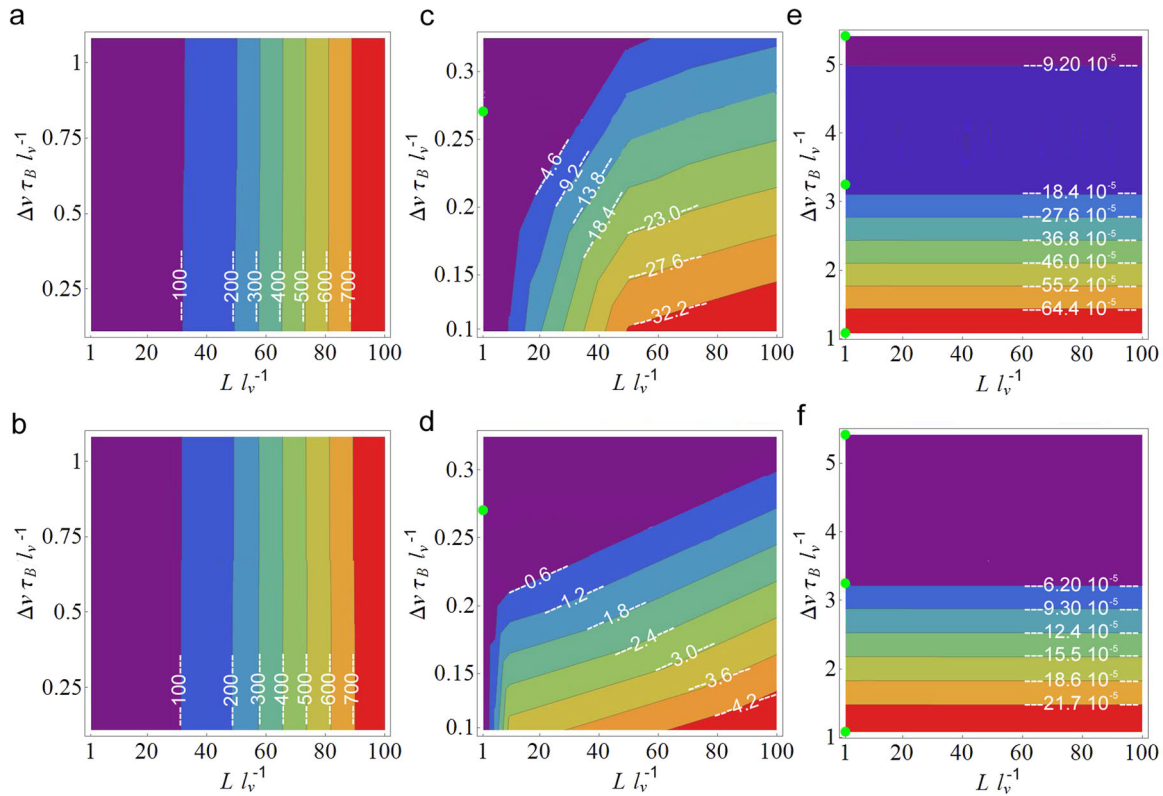


Fig. 7 Overview of localization scenarios for active particles in motility traps. As a measure of the efficiency of motility trapping, we numerically calculated the square of the scaled confinement length $\langle x^2 \rangle_{l_v}^{-2}$ encoded in color (values are shown inside each plot) as a function of $\Delta v \tau_B l_v^{-1}$ and $L l_v^{-1}$. Here, L is the box size and the trap length $\Delta v = v^{\max} - v^{\min}$, where v^{\max} and v^{\min} correspond to the respective maximal and minimal velocity. τ_B is the typical Brownian time. In all panels, the trap length is set to $l_v = 46.15 \sigma$, with σ the active particle (AP) diameter and $v^{\min} = 0$. Numerical simulations for a cooling and a heating map are shown in **a, c, e** and **b, d, f**, respectively. **a, b** Data in the absence of an active torque, that is, $c = 0$ (AP delocalization). **c-f** Data from numerical simulations in the presence of an active torque where $c = +0.6 \tau_B$ (**c, e**) and $c = -1.2 \tau_B$ (**d, f**) (AP localization). The green filled circles correspond to the experimental conditions presented in this work.

particle self-propulsion. In particular, active colloids generally respond to external gradients such as a chemical concentration gradient or a temperature field^{50,51}. Here, we exploit the close quantitative agreement between our model and experiments for APs in a motility trap to propose a simple inverse method to measure these coefficients.

For that purpose, we determine an analytical formula for the (tails of the) particle distribution in the motility trap, in the presence of an external gradient. Such a gradient couples to the orientation of nonuniform APs, yielding an additional term in Eq. (2), which then reads $\dot{\phi}(t) = \omega(\phi, x) + \sqrt{2D_r} \xi_\phi(t) - \beta_r C'(x) \sin \phi$. Here β_r is the coupling parameter to the external gradient and $C'(x)$ is the spatial derivative of an external field of the form $C(x) = hx + h_0$, which can represent, for example, a quasi one-dimensional external chemical concentration field (or the temperature field). Intuitively, it is clear that such an extra term leads to a bias of the particle distribution in the motility trap. This can also be seen formally, by generalizing our calculation of the particle distribution in the trap to account for the impact of the external field. The resulting distribution has the same form as Eq. (3) but with a different B (see “Methods” for calculation details)

$$B(x, h) = \left(\frac{v(x)}{v(0)} \right)^{\frac{h \beta_r}{v(x)}} \exp \left(-\frac{c}{\sigma} (v(x) - v(0)) + \frac{\beta_r h x}{v(x)} + \frac{h \beta_r}{v'(x)} \left(\frac{v(0)}{v(x)} - 1 \right) \right). \tag{9}$$

This distribution is biased in a way which uniquely depends on β_r (see “Methods”). We can now use this result for an indirect

measurement of coupling coefficients of APs to external gradients by (i) measuring the particle distribution in a motility trap, in the presence of a known external field $C(x)$ and (ii) matching the theoretically predicted distribution to the measured result. The latter step involves a matching of the flanks of the predicted distribution (Eqs. (3) and (9)) to the measured distribution in order to determine β_r .

Discussion

Our results suggest that motility-trapping provides a novel and generic scheme for the spatial confinement of APs. By specifically exploiting the flow field gradients around an AP in the presence of a motility gradient, this leads to a position-dependent re-alignment, which confines the AP close to the extremum of the motility landscape, that is, the trapping center. Importantly, this scheme does not require body forces that are typically used for particle localization. We emphasize that motility trapping, which has been exemplarily demonstrated for light-activated particles, will also apply to diffusiophoretic or thermophoretic APs in the presence of suitable chemical or thermal concentration profiles. It would also be interesting to generalize motility trapping to higher and in particular to three dimensions. This would avoid the additional influence of the substrate, which also modifies their behavior. In addition to the use of motility traps as a “motility tweezer,” our work also demonstrates how unknown coupling coefficients of APs to external field gradients (or gradients produced by other APs⁵⁰⁻⁵³) can be determined from the measured asymmetric particle probability distribution within a motility trap

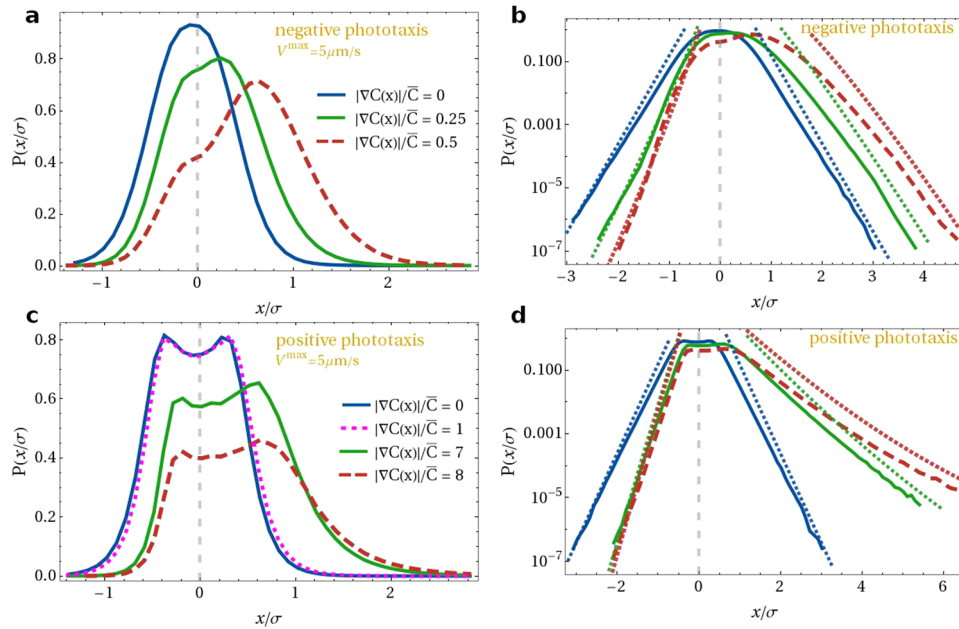


Fig. 8 Motility trap in the presence of additional external field gradients. Numerically calculated positional probability distributions of active particles (APs) in units of particle size σ confined to a motility trap with a superimposed external chemical gradient $\nabla C(x)$, where $C(x)$ is a linear chemical field. Different colors correspond to different strengths of the gradient, which is expressed in units of $\bar{C} = (2V^{\max}/l_v)^2 \tau_B/\beta_r$. The trap length is set to $l_v = 46.15 \sigma$, and the maximal velocity $V^{\max} = 5 \mu\text{m s}^{-1}$. τ_B is the typical Brownian time and β_r is the coupling parameter to the external chemical gradient. **a, b** Data for negative phototaxis and **c, d** for positive phototaxis. **b, d** show the same data as in **a, c**, but in semi-logarithmic representation and with the analytical noise-free probability distributions (Eq. (22)) superimposed as dotted lines with the same color as the simulation data.

in the presence of an additional external field (e.g., optical, thermal, or chemical gradient).

Methods

Creation of one-dimensional light patterns. Creation of triangle-shaped light fields is achieved by a line focus (widths of 1 and 2000 μm) of a laser beam ($\lambda = 532 \text{ nm}$), which is scanned within the sample plane with a frequency of 200 Hz. Synchronization of the scanning motion with the input voltage of an electro-optical modulator leads to user-defined one-dimensional illumination fields (see Fig. 2a)⁴⁶.

Particle tracking. Microscope images of the APs were taken with a frame rate of 12 fps and for a duration of at least 3600 s using a CCD camera. Particle positions $\mathbf{r} = (x, y)$ were obtained by automated in-house tracking routine developed with Matlab image analysis software, yielding a spatial resolution of $\sim 100 \text{ nm}$ ⁵⁴. Because of the optical contrast between the light-absorbing carbon cap and the otherwise transparent silica, the orientation of the cap is obtained from the vector connecting the particle center and the intensity centroid of the particle image. The error of this detection is $< 5\%$.

AP reorientational dynamics within light gradients. The AP's reorientation dynamics in an intensity gradient ∇I is (in the absence of noise) described by the differential Eq. (2). Solving this equation gives $\cos \phi(t) = \tanh(\omega_{\max}(\bar{t} - t))$, where \bar{t} is the time when $\phi(\bar{t}) = \pi/2$ and $\omega_{\max} \propto \nabla I$ is the only fitting parameter used to obtain the theoretical fit in Fig. 3a and which strongly depends on ∇I ⁴⁶. From this, one obtains the reorientation time $\tau = \frac{2}{\omega_{\max}} \ln\left(\frac{\cos(\phi_{\omega_{\max}}) + 1}{\sin(\phi_{\omega_{\max}})}\right)$, where $\phi_{\omega_{\max}}$ is the total rotation⁴⁶. The reorientation times given in the paper correspond to the value for $\phi_{\omega_{\max}} = 3 \text{ rad}$, which is shown in Fig. 3a, b vs. ∇I ⁴⁶.

Brownian dynamics simulations. We have solved the equations of motion by using Brownian dynamics computer simulations with periodic boundary condition along x direction. In our simulations, we use the Brownian time $\tau_B = \sigma^2/D$ and the diameter of the particle σ as time and length units. In line with the experiments, we choose $l_v = 46.15 \sigma$ and $V^{\max} = 12.5, 50, 150, \text{ and } 250 \sigma/\tau_B$, and $V^{\min} = 0$. According to our experiments, the prefactor c is chosen to be $c = +0.6$ and $-1.2\tau_B$ for negative and positive phototaxis, respectively.

Particle distribution in the trap. Here, we derive a simple analytical expression for the particle distribution function (or its density profile) in the trap. Let us discuss this for motility profiles $v(x)$, which are piecewise linear in x . For negative phototaxis (cooling trap), the self-propulsion speed of the particles, in line with the

light-intensity profile in our experiments, is approximated as

$$v(x) = \begin{cases} 2 \frac{V^{\max} - V^{\min}}{l_v} |x| + V^{\min}, & |x| \leq l_v/2, \\ V^{\max}, & \text{else,} \end{cases} \quad (10)$$

where l_v is the size of the trap, $V^{\max} - V^{\min}$ defines its depth, and $V^{\min} < V^{\max}$ is a general background motility. Likewise, for positive phototaxis (heating trap), the profile is inverted such that we assume

$$v(x) = \begin{cases} -2 \frac{V^{\max} - V^{\min}}{l_v} |x| + V^{\max}, & |x| \leq l_v/2, \\ V^{\min}, & \text{else.} \end{cases} \quad (11)$$

Neglecting noise in the basic equations of motion (Eq. (1) and Eq. (2)) yields for $x(t)$ and $\phi(t)$

$$\dot{x} = v(x) \cos(\phi), \quad (12)$$

and

$$\dot{\phi} = \frac{c}{\sigma} v(x) v'(x) \sin(\phi). \quad (13)$$

By dividing these two equations, we obtain

$$\frac{d\phi}{dx} = \frac{c v'(x)}{\sigma \cot(\phi)}. \quad (14)$$

Integration of Eq.(14) yields the relation

$$\begin{aligned} \phi(x) &= \arcsin\left(\sin(\phi_0) \exp\left(\frac{c}{\sigma} (v(x) - v(0))\right)\right) \\ &= \arcsin\left(\sin(\phi_0) e^{\frac{2c(V^{\max} - V^{\min})}{\sigma l_v} (|x| - |x_0|)}\right), \end{aligned} \quad (15)$$

for any given initial condition $x_0 = x(0)$ and $\phi_0 = \phi(0)$. Let us now obtain a condition for the maximal excursion X_m of the particle from the trap center. A maximal excursion implies that the particle orientation is exactly $\pi/2$, hence $\phi(x = X_m) = \pi/2$. Plugging this into Eq. (15) we obtain the relation

$$\pi/2 = \arcsin\left(\sin(\phi_0) e^{\frac{2c(V^{\max} - V^{\min})}{\sigma l_v} (|X_m| - |x_0|)}\right),$$

which we can solve for X_m as

$$|X_m| = |x_0| + \frac{\sigma l_v}{2|c|(V^{\max} - V^{\min})} \ln\left(\frac{1}{\sin(\phi_0)}\right). \quad (16)$$

Consequently, the critical initial orientation angle ϕ_c needed to reach the size of the trap when starting inside the trap ($x_0 = 0$) is given implicitly by $X_m(\phi_c) = l_v/2$,

which yields

$$\phi_c = \phi_0(X_m = l_v/2) = \arcsin(e^{-|c|\Delta v/\sigma}). \quad (17)$$

Now to obtain the particle distribution $P(x)$ in the trap, we make two assumptions. First, we assume that the particle orientation is almost homogeneously distributed when the particle is in the trap center. This first assumption is reasonable since there is no torque when $x_0 = 0$ and noise leads to a further smearing of orientations. Moreover, this assumption is found in our simulations to a large extent. Second, we assume that the main weight in the particle distribution $P(x)$ is given by the particle trajectory when it is stationary in x , that is, when it is turning at $x = X_m$. In particular, this is a good approximation for the wings of the particle distribution, which are dominated by the turning events. Consequently, we set $P(x) \approx \tilde{P}(X_m)$, where $\tilde{P}(X_m)$ is the distribution of the maximal excursions. The homogeneous distribution of initial angles then simply transforms into $\tilde{P}(X_m)$ via

$$\tilde{P}(X_m) = \frac{1}{\pi} \left| \frac{d\phi_0}{dX_m} \right| = \frac{2|c|(V^{\max} - V^{\min})}{\sigma \pi l_v} \frac{\exp\left(-2 \frac{|c|(V^{\max} - V^{\min})}{\sigma l_v} |X_m|\right)}{\sqrt{1 - \exp\left(-4 \frac{|c|(V^{\max} - V^{\min})}{\sigma l_v} |X_m|\right)}}, \quad (18)$$

which directly yields Eq. (3).

These trapping mechanisms can be used as a sensor of an external field. Specifically, in case of chemotactic rotational motion in the vicinity of the chemical field $C(x)$, the rotational Langevin Eq. (2) goes to

$$\dot{\phi}(t) = \frac{c}{\sigma} v(x) v'(x) \sin \phi + \sqrt{2D_r} \xi_\phi(t) - \beta_r C'(x) \sin \phi, \quad (19)$$

where $\beta_r(r)$ denotes the rotational chemotactic coupling coefficient. Therefore, in case of vanishing noise, the relation between $\phi(t)$ and $x(t)$ is obtained as

$$\begin{aligned} \sin(\phi(x)) &= \sin(\phi_0) \exp\left(2 \frac{c \Delta v}{\sigma l_v} (|x| - |x_0|) - \beta_r \frac{C(x)}{v(x)}\right) \\ &+ \beta_r \frac{C(x_0)}{v(x_0)} - \beta_r \int_{x_0}^x dx' \frac{C(x')}{v^2(x')} v'(x'), \end{aligned} \quad (20)$$

which yields Eq. (15) when $\beta_r = 0$. That is to say, by knowing $C(x)$ and solving the integral on r.h.s., one can find the probability distribution $P(x)$ in the presence of chemotaxis. For instance, in case of a linear chemical field $C(x) = hx + h_0$, Eq. (20) goes to

$$\sin(\phi(x)) = \sin(\phi_0) \left(\frac{v(0)}{v(x)}\right)^{\frac{h\beta_r}{v'(0)}} \exp\left(\frac{c}{\sigma}(v(x) - v(0)) - \beta_r \frac{hx}{v(x)} - \frac{h\beta_r}{v'(x)} \left(\frac{v(0)}{v(x)} - 1\right)\right), \quad (21)$$

with $x_0 = 0$. Following the same assumptions and similar calculations giving rise to the derivation of Eq. (3) from Eq. (15), Eq. (21) yields the noise-free probability distribution in the vicinity of the linear chemical field

$$P(x) \simeq \frac{\pi^{-1} \left| \frac{dB(x,h)}{dx} \right|}{\sqrt{1 - B^2(x,h)}}, \quad (22)$$

with $B(x, h)$ given by Eq. (9). This probability distribution is biased due to the presence of the external chemical gradient. It can be used for indirect measurements of coupling coefficients of APs to external gradients (or gradients produced by other APs^{50–53}). This can be done by measuring the AP distribution in a motility trap in the presence of an additional external chemical gradient (or analogously a thermal or intensity gradient). When matching the flanks of the predicted distribution (Eq. (22)), which depend uniquely on β_r (Fig. 8) to the measured ones, this allows to determine β_r . In Fig. 8, we show the AP distribution for different reduced chemical gradients $|\nabla C|/\bar{C}$, where $\bar{C} = (2V^{\max}/l_v)^2 \tau_B/\beta_r$.

Data availability

The data that support the findings of this study are available from the corresponding author upon reasonable request.

Code availability

The code that supports the findings of this study are available from the corresponding author upon request.

Received: 9 March 2020; Accepted: 18 June 2020;

Published online: 14 July 2020

References

- Anderson, M. H., Ensher, J. R., Matthews, M. R., Wieman, C. E. & Cornell, E. A. Observation of Bose–Einstein condensation in a dilute atomic vapor. *Science* **269**, 198–201 (1995).
- Davis, K. B., Mewes, M.-O., Joffe, M. A., Andrews, M. R. & Ketterle, W. Evaporative cooling of sodium atoms. *Phys. Rev. Lett.* **75**, 2909 (1995).
- Davis, K. B. et al. Bose–Einstein condensation in a gas of sodium atoms. *Phys. Rev. Lett.* **75**, 3969–3973 (1995).
- Cirac, J. I. & Zoller, P. Quantum computations with cold trapped ions. *Phys. Rev. Lett.* **74**, 4091–4094 (1995).
- Blatt, R. & Wineland, D. Entangled states of trapped atomic ions. *Nature* **453**, 1008–1015 (2008).
- Ashkin, A. & Dziedzic, J. M. Optical trapping and manipulation of viruses and bacteria. *Science* **235**, 1517–1520 (1987).
- Grier, D. G. A revolution in optical manipulation. *Nature* **424**, 810–816 (2003).
- Wang, M. D., Yin, H., Landick, R., Gelles, J. & Block, S. M. Stretching DNA with optical tweezers. *Biophys. J.* **72**, 1335–1346 (1997).
- Bechinger, C. et al. Active particles in complex and crowded environments. *Rev. Mod. Phys.* **88**, 045006 (2016).
- Marchetti, M. C. et al. Hydrodynamics of soft active matter. *Rev. Mod. Phys.* **85**, 1143–1189 (2013).
- Zöttl, A. & Stark, H. Emergent behavior in active colloids. *J. Phys. Condens. Matter* **28**, 253001 (2016).
- Ebbens, S. J. Active colloids: progress and challenges towards realising autonomous applications. *Curr. Opin. Colloid Interface Sci.* **21**, 14–23 (2016).
- Ginot, F., Theurkauff, I., Detcher, F., Ybert, C. & Cottin-Bizonne, C. Aggregation–fragmentation and individual dynamics of active clusters. *Nat. Commun.* **9**, 696 (2018).
- Paxton, W. F. et al. Catalytic nanomotors: autonomous movement of striped nanorods. *J. Am. Chem. Soc.* **126**, 13424–13431 (2004).
- Jiang, H.-R., Yoshinaga, N. & Sano, M. Active motion of a Janus particle by self-thermophoresis in a defocused laser beam. *Phys. Rev. Lett.* **105**, 268302 (2010).
- Elgeti, J., Winkler, R. G. & Gompper, G. Physics of microswimmers—single particle motion and collective behavior: a review. *Rep. Prog. Phys.* **78**, 056601 (2015).
- Lozano, C. & Bechinger, C. Diffusing wave paradox of phototactic particles in traveling light pulses. *Nat. Commun.* **10**, 2495 (2019).
- Palacci, J. et al. Artificial rheotaxis. *Sci. Adv.* **1**, e1400214 (2015).
- Lavergne, F. A., Wendehenne, H., Bäuerle, T. & Bechinger, C. Group formation and cohesion of active particles with visual perception-dependent motility. *Science* **364**, 70–74 (2019).
- Bäuerle, T., Fischer, A., Speck, T. & Bechinger, C. Self-organization of active particles by quorum sensing rules. *Nat. Commun.* **9**, 3232 (2018).
- Ma, X., Hahn, K. & Sanchez, S. Catalytic mesoporous Janus nanomotors for active cargo delivery. *J. Am. Chem. Soc.* **137**, 4976–4979 (2015).
- Demirörs, A. F., Akan, M. T., Poloni, E. & Studart, A. R. Active cargo transport with Janus colloidal shuttles using electric and magnetic fields. *Soft Matter* **14**, 4741–4749 (2018).
- Mano, T., Delfau, J.-B., Iwasawa, J. & Sano, M. Optimal run-and-tumble-based transportation of a Janus particle with active steering. *Proc. Natl Acad. Sci. USA* **114**, E2580–E2589 (2017).
- Kumar, N., Gupta, R. K., Soni, H., Ramaswamy, S. & Sood, A. K. Trapping and sorting active particles: motility-induced condensation and smectic defects. *Phys. Rev. E* **99**, 032605 (2019).
- Guidobaldi, A. et al. Geometrical guidance and trapping transition of human sperm cells. *Phys. Rev. E* **89**, 032720 (2014).
- Restrepo-Pérez, L., Soler, L., Martínez-Cisneros, C. S., Sánchez, S. & Schmidt, O. G. Trapping self-propelled micromotors with microfabricated chevron and heart-shaped chips. *Lab Chip* **14**, 1515–1518 (2014).
- Thalhammer, G. et al. Combined acoustic and optical trapping. *Biomed. Opt. Express* **2**, 2859 (2011).
- Dauchot, O. & Démery, V. Dynamics of a self-propelled particle in a harmonic trap. *Phys. Rev. Lett.* **122**, 068002 (2019).
- Simmchen, J. et al. Topographical pathways guide chemical microswimmers. *Nat. Commun.* **7**, 10598 (2016).
- Volpe, G., Buttinoni, I., Vogt, D., Kümmerer, H.-J. & Bechinger, C. Microswimmers in patterned environments. *Soft Matter* **7**, 8810 (2011).
- Kaiser, A., Wensink, H. H. & Löwen, H. How to capture active particles. *Phys. Rev. Lett.* **108**, 268307 (2012).
- Jones, P., Marago, O. & Volpe, G. *Optical Tweezers: Principles and Applications* (Cambridge Univ. Press, Cambridge, 2015).
- Liu, J. & Li, Z. Controlled mechanical motions of microparticles in optical tweezers. *Micromachines* **9**, 232 (2018).
- Zong, Y. et al. An optically driven bistable Janus rotor with patterned metal coatings. *ACS Nano* **9**, 10844–10851 (2015).
- Nedev, S. et al. An optically controlled microscale elevator using plasmonic Janus particles. *ACS Photonics* **2**, 491–496 (2015).
- Liu, J., Guo, H.-L. & Li, Z.-Y. Self-propelled round-trip motion of Janus particles in static light optical tweezers. *Nanoscale* **8**, 19894–19900 (2016).

37. Moyses, H., Palacci, J., Sacanna, S. & Grier, D. G. Trochoidal trajectories of self-propelled Janus particles in a diverging laser beam. *Soft Matter* **12**, 6357–6364 (2016).
38. Mousavi, S. M. et al. Clustering of Janus particles in an optical potential driven by hydrodynamic fluxes. *Soft Matter* **15**, 5748–5759 (2019).
39. Bregulla, A. P., Yang, H. & Cichos, F. Stochastic localization of microswimmers by photon nudging. *ACS Nano* **8**, 6542–6550 (2014).
40. Takatori, S. C., De Dier, R., Vermant, J. & Brady, J. F. Acoustic trapping of active matter. *Nat. Commun.* **7**, 10694 (2016).
41. Soto, R. & Golestanian, R. Run-and-tumble dynamics in a crowded environment: persistent exclusion process for swimmers. *Phys. Rev. E* **89**, 012706 (2014).
42. Howse, J. R. et al. Self-motile colloidal particles: from directed propulsion to random walk. *Phys. Rev. Lett.* **99**, 048102 (2007).
43. Gomez-Solano, J. R. et al. Tuning the motility and directionality of self-propelled colloids. *Sci. Rep.* **7**, 14891 (2017).
44. Buttinoni, I., Volpe, G., Kümmel, F., Volpe, G. & Bechinger, C. Active Brownian motion tunable by light. *J. Phys. Condens. Matter* **24**, 284129 (2012).
45. Samin, S. & van Roij, R. Self-propulsion mechanism of active Janus particles in near-critical binary mixtures. *Phys. Rev. Lett.* **115**, 188305 (2015).
46. Lozano, C., Ten Hagen, B., Löwen, H. & Bechinger, C. Phototaxis of synthetic microswimmers in optical landscapes. *Nat. Commun.* **7**, 12828 (2016).
47. Anderson, J. Colloid transport by interfacial forces. *Annu. Rev. Fluid Mech.* **21**, 61–99 (1989).
48. Phillips, W. D. Laser cooling and trapping of neutral atoms. *Rev. Mod. Phys.* **40**, <https://doi.org/10.21236/ada253730> (1992).
49. Cates, M. E. & Tailleur, J. Motility-induced phase separation. *Annu. Rev. Condens. Matter Phys.* **6**, 219–244 (2015).
50. Liebchen, B. & Löwen, H. Synthetic chemotaxis and collective behavior in active matter. *Acc. Chem. Res.* **51**, 2982–2990 (2018).
51. Saha, S., Golestanian, R. & Ramaswamy, S. Clusters, asters, and collective oscillations in chemotactic colloids. *Phys. Rev. E* **89**, 062316 (2014).
52. Liebchen, B., Marenduzzo, D., Pagonabarraga, I. & Cates, M. E. Clustering and pattern formation in chemorepulsive active colloids. *Phys. Rev. Lett.* **115**, 258301 (2015).
53. Pohl, O. & Stark, H. Dynamic clustering and chemotactic collapse of self-phoretic active particles. *Phys. Rev. Lett.* **112**, 238303 (2014).
54. Lozano, C., Gomez-Solano, J. R. & Bechinger, C. Run-and-tumble-like motion of active colloids in viscoelastic media. *N. J. Phys.* **20**, 015008 (2018).

Acknowledgements

C.B. acknowledges financial support by the ERC Advanced Grant ASCIR (Grant No. 693683). C.B. and H.L. acknowledge support from the German Research Foundation (DFG) through the priority program SPP 1726.

Author contributions

C.L., C.B., and H.L. have planned the project. S.J./B.L. and C.L. have performed the theoretical and experimental research, respectively. All authors have discussed and interpreted the results and have written and edited the manuscript.

Competing interests

The authors declare no competing interests.

Additional information

Correspondence and requests for materials should be addressed to C.B.

Reprints and permission information is available at <http://www.nature.com/reprints>

Publisher's note Springer Nature remains neutral with regard to jurisdictional claims in published maps and institutional affiliations.



Open Access This article is licensed under a Creative Commons

Attribution 4.0 International License, which permits use, sharing, adaptation, distribution and reproduction in any medium or format, as long as you give appropriate credit to the original author(s) and the source, provide a link to the Creative Commons license, and indicate if changes were made. The images or other third party material in this article are included in the article's Creative Commons license, unless indicated otherwise in a credit line to the material. If material is not included in the article's Creative Commons license and your intended use is not permitted by statutory regulation or exceeds the permitted use, you will need to obtain permission directly from the copyright holder. To view a copy of this license, visit <http://creativecommons.org/licenses/by/4.0/>.

© The Author(s) 2020